Article:
Frost, DA, Garnero, EJ and Rost, S (2018) Dynamical links between small- and large-scale mantle heterogeneity: seismological evidence. Earth and Planetary Science Letters, 482. pp. 135-146. ISSN: 0012-821X

https://doi.org/10.1016/j.epsl.2017.10.058

Title: Dynamical links between small- and large-scale mantle heterogeneity: seismological evidence

Authors: Daniel A. Frost[1]*, Edward J. Garnero[2], and Sebastian Rost[3]

Affiliations:

[1]Earth & Planetary Science, University of California, Berkeley, California, USA

[2]School of Earth and Space Exploration, Arizona State University, Tempe, Arizona, USA

[3]Institute of Geophysics and Tectonics, School of Earth and Environment, University of Leeds, Leeds, UK

*Correspondence to: dafrost@berkeley.edu

Abstract

We identify PKP•PKP scattered waves (also known as P′•P′) from earthquakes recorded at small-aperture seismic arrays at distances less than 65°. P′•P′ energy travels as a PKP wave through the core, up into the mantle, then scatters back down through the core to the receiver as a second PKP. P′•P′ waves are unique in that they allow scattering heterogeneities throughout the mantle to be imaged. We use array-processing methods to amplify low amplitude, coherent scattered energy signals and resolve their incoming direction. We deterministically map scattering heterogeneity locations from the core-mantle boundary to the surface. We use an

extensive dataset with sensitivity to a large volume of the mantle and a location method allowing us to resolve and map more heterogeneities than have previously been possible, representing a significant increase in our understanding of small-scale structure within the mantle. Our results demonstrate that the distribution of scattering heterogeneities varies both radially and laterally. Scattering is most abundant in the uppermost and lowermost mantle, and a minimum in the mid-mantle, resembling the radial distribution of tomographically derived whole-mantle velocity heterogeneity. We investigate the spatial correlation of scattering heterogeneities with large-scale tomographic velocities, lateral velocity gradients, the locations of deep-seated hotspots and subducted slabs. In the lowermost 1500 km of the mantle, small-scale heterogeneities correlate with regions of low seismic velocity, high lateral seismic gradient, and proximity to hotspots. In the upper 1000 km of the mantle there is no significant correlation between scattering heterogeneity location and subducted slabs. Between 600 and 900 km depth, scattering heterogeneities are more common in the regions most remote from slabs, and close to hotspots. Scattering heterogeneities show an affinity for regions close to slabs within the upper 200 km of the mantle. The similarity between the distribution of large-scale and small-scale mantle structures suggests a dynamic connection across scales, whereby mantle heterogeneities of all sizes may be directed in similar ways by large-scale convective currents.

Keywords: seismology; deep Earth; scattering; mantle structure; mantle dynamics; seismic arrays

1. Introduction

The high frequency (~1 Hz) seismic wavefield provides evidence of kilometre scale structure within the Earth [Cleary and Haddon, 1972]. Seismic energy that is not explained by wave propagation in smoothly varying velocity models of the Earth has been attributed to reflections and scattering from sharply contrasting volumetric heterogeneities and roughness on interfaces [Chang and Cleary, 1981]. The interaction of the wavefield with discrete, small-scale variations in elastic properties and/or density can divert seismic energy onto new paths, often generating precursors or postcursors (coda) to the main seismic phases that travel in the great circle plane. The size of the scatterers that can be imaged is dependent upon the wavelength that is analysed; for the teleseismic high-frequency P-wavefield above 1 Hz they are typically on the order of 1 to 10 km.

Global imaging of Earth's small-scale heterogeneities is difficult due to the uneven distribution of earthquake sources and seismic receivers, and the low amplitude of the scattered signals involved. Scattering can be studied using single stations, but with this approach the location of the scattering heterogeneity can be ambiguous [Wen, 2000]. Alternatively, seismic arrays, i.e., 3 or more closely located sensors, can resolve the incoming direction of scattered waves, thus it is possible to deterministically locate heterogeneities [Thomas et al., 1999; Rost and Earle, 2010; Frost et al., 2013]. In the last few decades a number of studies have started to unravel the distribution of small-scale heterogeneities of Earth's mantle. Hedlin et al. [1997], and later Mancinelli and Shearer [2013, 2016] studied the depth distribution of heterogeneity within the mantle through analysis of PKP pre- and postcursors recorded at single stations. Using a stochastic Rayleigh-Born scattering

73 approach, Mancinelli and Shearer [2013, 2016] developed a global model of
74 scattering heterogeneity containing 0.1% root-mean-square velocity variations in
75 the deepest 1200 km of the mantle with heterogeneity scale sizes ranging from 2 to
76 30 km.

77 This work is complemented by studies that deterministically map small-scale
78 scattering heterogeneity within the upper and lower mantle. These studies have
79 noted lateral variations in heterogeneity distribution, as well as variations in
80 amplitudes of scattered waves. Scattered P-to-P (P•P, where the "•" represents the
81 location of scattering) and P-to-S (P•S) waves are sensitive to heterogeneities in the
82 upper half of Earth's mantle; they have been used to map scattering heterogeneity in
83 regions influenced by recent subduction [Kaneshima and Helffrich, 1998; Bentham
84 and Rost, 2014]. Scattering in the lowermost mantle has also been observed to vary
85 laterally [Waszek et al., 2015]. Strong scattering has been observed in regions
86 beneath mantle hotspots [Wen, 2000], near small, regional ultra-low velocity zone
87 (ULVZ) structures [Yao and Wen, 2014], beneath subduction zones [Miller and Niu,
88 2008], and near the edges of LLSVPs [Frost et al., 2013]. A near-global study of
89 PK•KP – a PKP wave that is back-scattered in the lower mantle onto a second PKP
90 path – suggests a spatial correlation between scattering and LLSVP edges in the
91 lowermost 300 km of the mantle [Rost and Earle, 2010; Frost et al., 2017].

92 The volume of the mantle that can be investigated for scattering
93 heterogeneity is controlled by the specifics of the seismic probe. PK•KP can be used
94 to investigate the lower mantle close to the CMB [Chang and Cleary, 1981; Rost and
95 Earle, 2010; Frost et al., 2017]. The direct wave PKPPKP (also called P′P′) results

96 from a PKP wave (P′) reflecting from the underside of the surface, back into the
97 Earth as a second PKP wave, along the great-circle path (GCP). This phase can be
98 preceded by scattered energy called PKP•PKP (P′•P′), caused by back-scattering of
99 PKP at any depth in the mantle [Rost et al., 2015]. Like PK•KP, P′•P′ has an unusual
100 scattering geometry (Fig. 1) and can scatter from locations off the GCP, and the P′
101 segments need not be symmetric to each other. P′•P′ is the continuation of PK•KP
102 towards the surface, thus this phase is able to sample the whole mantle from CMB to
103 crust (Fig. 2). We extend our earlier work and investigate the mantle upwards from
104 the CMB to the surface to deterministically map the vertical and lateral distribution
105 of scattering heterogeneities throughout the mantle. In contrast to other scattering
106 probes, the unusual (and versatile) raypath geometry of P′•P′ allows the study of
107 previously unsampled regions of the Earth.

108 The internal structure of the Earth and the nature of mantle convection are
109 inherently connected across scales [e.g. Tackley 2015]. The distribution of large-
110 scale mantle structure as imaged by seismic tomography has been investigated
111 using thermo-chemical geodynamic models, which indicate that downwelling of cold,
112 dense slabs at subduction zones moves and shapes the hot, convecting piles of
113 seismically slow material at the CMB, forming the Large Low Shear Velocity
114 Provinces (LLSVPs) [McNamara and Zhong, 2005; Li et al., 2014; Domeier et al,
115 2016]. The LLSVPs, if compositionally distinct, may modulate mantle dynamics
116 through thermal instabilities that result in mantle plumes that rise up causing
117 hotspot volcanism [Thorne et al., 2004; French and Romanowicz, 2015].
118 Furthermore, calculations suggest that mantle plumes may be spatially correlated

119 with the LLSVPs [Thorne et al., 2004; Doubrovine et al., 2016]. Geodynamic
120 modelling of thermo-chemical structures in the deep mantle indicates that small-
121 scale heterogeneities (as small as kilometre-sized) can be passively transported in
122 the large-scale flow [Brandenburg and van Keken, 2007; Li et al., 2014, Mulyukova
123 et al., 2015]. Furthermore, geochemical analysis of intraplate volcanism suggests
124 that heterogeneities situated in the deep Earth may be transported to the surface by
125 entrainment in mantle convection [Williams et al., 2015]. Therefore, there is
126 compelling evidence that the distribution of small-scale seismic structure in the
127 mantle is linked to the large-scale structures.

128 Here we use a global collection of earthquakes recorded at seismic arrays to
129 identify P′•P′ and deterministically locate the position of the causative volumetric
130 scattering heterogeneity within the mantle. We investigate the relationship between
131 scattering heterogeneity and other seismologically imaged structures in the mantle.
132 We use our observations to understand the distribution of small-scale
133 heterogeneities throughout the whole of the mantle, and the connection with
134 dynamic processes.

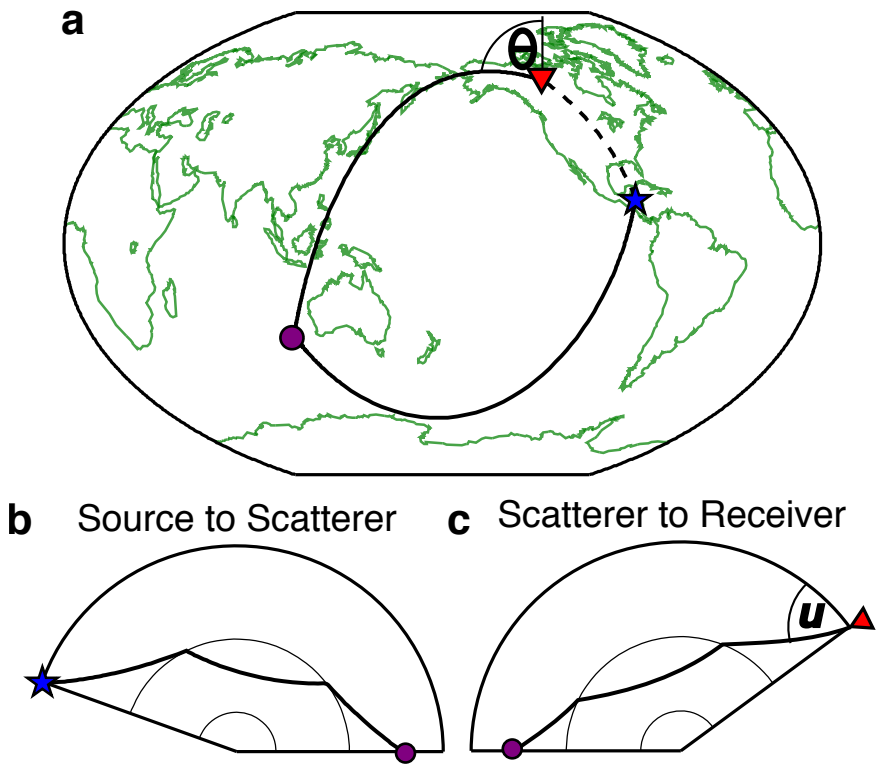

Figure 1: PKP•PKP (P′•P′) example path. **(a)** A P′•P′ path from the source (star) to a scattering point in the mantle (circle) and then to the receiver (triangle). P′•P′ travels along two great-circle paths (solid lines) to and from the scattering point, off the great-circle path between the source and receiver (dashed line). PKP ray paths from **(b)** source to scatterer (PKP_{ab}) and **(c)** scatterer to receiver (PKP_{bc}). The two PKP legs may be symmetric or asymmetric (as in this case) and can scatter from any depth in the mantle from the CMB to the surface. Rays observed at the surface arrive from a specific direction known as the back-azimuth, θ, measured relative to North, or the relative back-azimuth measured from the GCP, and from a vertical incidence angle, referred to as the slowness, *u*.

[SINGLE OR 1.5 COLUMN FIGURE]

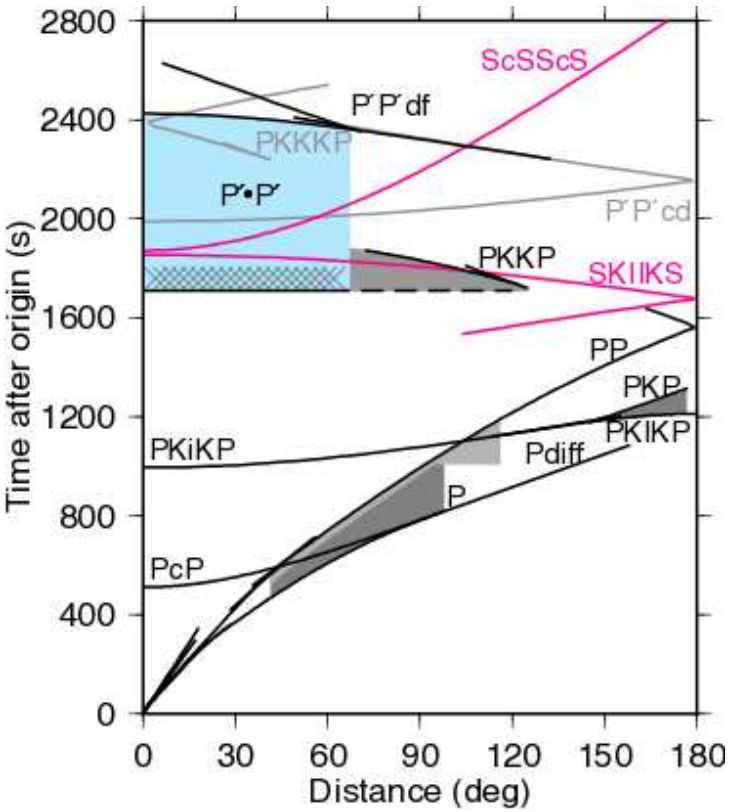

Figure 2: Travel-time curve displaying P′•P′ and other scattered phases in the high-frequency seismic wavefield. Black lines mark major P-wave phases. The blue region marks the time and distance region investigated for P′•P′ waves in this study. Hatched region marks time and distance region investigated for PK•KP in Frost et al., [2017]. Grey and pink lines mark the P- and S-waves, respectively, that may contaminate the P′•P′ study region. Other P- and S-waves are not shown for clarity. Differently shaded grey regions denote time and distance regions previously investigated for other scattered waves. Adapted from Rost et al., [2015].

[SINGLE COLUMN FIGURE]

2. Data

We collect data from 643 earthquakes at any depth with magnitudes M≥6 recorded at up to 12 small and medium aperture arrays within 65° of any event (Fig. 3). The arrays contain a mixture of short period and broadband instruments; we use only the most common instrument type in each array. These arrays were designed

to determine the directivity of short-period P-waves thus are ideally suited for analysis of high-frequency scattered waves. The aperture of an array controls its directivity resolution, thus we select only arrays with apertures of 10km to 30 km to ensure that we are able to resolve well the incoming direction of waves.

Each event-array pair has a specific geographical volume of the mantle from which possible P′•P′ scattered waves can be detected (Fig. 3). The size and shape of the sampling region at any given scattering depth is dependent on the event-array distance. Using estimations of the potential scattering volumes combined for all source-array pairs, we develop a "potential sampling density map" of our dataset for different depths, which represents the abundance of scatterers we would detect if the actual distribution of scattering in the Earth distribution were uniform. The potential scatterer sampling distribution of the dataset is uneven, but in contrast to other probes, the southern hemisphere is well covered throughout the depth of the mantle, allowing investigation of the relationship between scattering heterogeneities and the South and Central American subduction zones, and the African and Pacific LLSVPs.

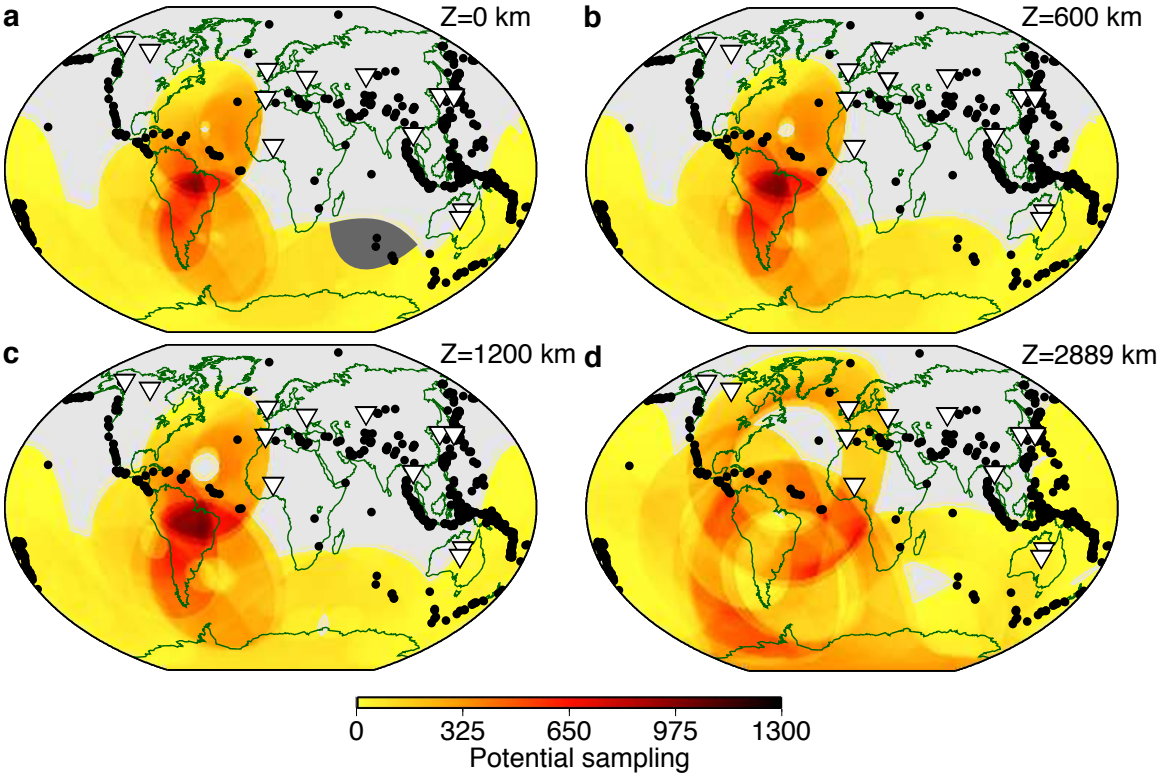

Figure 3: Earthquakes (dots) and arrays (triangles) in our dataset and resultant potential P′•P′ scattering sampling. The 643 events and up to 12 arrays yielded 1715 event-array pairs. Global sampling distributions are constructed by summation of the potential scattering sampling for all source-array pairs at: **(a)** the surface (0 km depth); **(b)** transition zone (600 km depth); **(c)** mid-mantle (1200 km depth); and **(d)** the Core-Mantle Boundary (2889 km depth). Sampling is densest in the mid-mantle and most geographically extensive in the lowermost mantle. Grey wedge in **(a)** displays an example of the potential scattering regions for a single event-array pair.

[2 COLUMN FIGURE]

3. Methods

We investigate energy associated with mantle scattering in a time window from the first possible arrival of P′•P′ at ~1700s after the earthquake origin time (for a surface focus event) corresponding to scattering at the CMB, up to the first

possible arrival of the direct wave $P'•P'_{df}$ at ~2400s, which is the earliest P′•P′ GCP phase, reflecting from the underside of the surface on the antipodal side (Fig. 2). P′•P′ scattering related to interactions with small-scale mantle heterogeneity is feasible for any time and distance in this window (blue shaded region in Fig. 2).

We de-trend the data and discard any discontinuous traces i.e. gaps in the recording. The remaining traces are filtered with a 2nd order bandpass between 0.5 and 2 Hz to enhance the frequencies most associated with small-scale scattering in past studies that investigated frequency content [Mancinelli et al., 2016; Frost et al., 2017]. We search for scattered signals within the wavefield data using fk-analysis (frequency-wavenumber), which performs a grid-search over incoming directions to maximise coherence (the similarity of two or more signals in the frequency domain) of the signal stacked across the array, calculated in the frequency domain [Capon, et al., 1967]. We search over slownesses from 0 to 8 sec/deg and back-azimuths between -180° to 180° relative to the GCP. By selecting signals with the highest coherence we determine the best fitting slowness vector (a combination of the back-azimuth, θ, and the horizontal slowness, $\underline{u}$) of the incoming signals in the scattering search time-window (1700s to 2400s after earthquake origin). To improve the resolution of the slowness vector of incoming signals, as well as to further increase the prominence of signals above the noise, we apply the F-statistic to the fk-analysis (Fig. 4) [Blandford, 1974; Selby, 2011]. The F-statistic calculates the ratio of the amplitude of the stacked signal to the sum of the differences between the stack and each trace used to form the stack. The F-trace has the effect of penalising stacks that differ from individual input traces i.e. signals that are

incoherent across the array. Thus, the best fitting slowness and back-azimuth from the grid-search are those that produce the most representative stack of the individual array traces. By performing these calculations in the frequency domain we increase efficiency by reducing the number of transformations required between the time and frequency domains. However, the fk approach returns a single value of coherence from each slowness vector averaged across the whole time window, thus collapsing the time axis. Combining the F-statistic with traditional fk-analysis results in much-improved slowness vector resolution, even for the small-aperture arrays used here [Frost et al., 2013]. Thus the origin of the scattered energy can be more precisely estimated.

We measure the slowness and back-azimuth of the most coherent signals received at the array in consecutive 50 s long time windows (Fig. 4). This window length gives depth resolution comparable to that obtained in global tomography models, and is sufficient to identify broad-scale trends in scattering distribution, both laterally and with depth. We assume the arrival time of a signal to be the middle of the 50 s time window, and given that scattering of P′•P′ from a range of depths can arrive at the array with similar travel-times, each 50 s time window that we investigate is sensitive to scattering from a 50 to 200 km thickness of the mantle. The thickness of the scattering region that each time window is sensitive to decreases with scattering depth hence, at shallower depths, there is overlap in depth sensitivity between windows – adjacent time windows can contain energy scattered from the same depth (albeit from different locations).

Mantle scattered P′•P′ waves are expected to arrive with slownesses between 2.1 and 4.4 s/deg. The range of directions from which P′•P′ waves can be observed is dependent upon the event-array distance and scattering depth. Array analyses permit recognition and omission of contaminating waves by determination of the incoming direction of energy, compared with the directions possible for P′•P′. We compute the expected arrival times for possible contaminating waves: direct phases, depth phases, and multiple reflections of both P- and S-waves. We do not calculate multiples reflecting off upper mantle discontinuities (i.e. a downgoing wave reflecting off the 660 km discontinuity, then reflecting back down from the 410 km discontinuity). Contaminating waves would likely be detected along the GCP (we take both minor and major arc arrivals into account). In contrast, P′•P′ scattered energy most commonly arrives off the GCP, allowing clear identification of the scattered arrivals. However, at short event-array distances it is possible for P′•P′ to arrive along the GCP; these situations can be predicted and extra care is taken to exclude contaminating phases. As there are few phases that can arrive within the P′•P′ window (Fig 2), we would expect few time windows to be contaminated by other seismic phases. Nonetheless, we discard any time window where we both observe a signal within 20 degrees of the GCP (in major or minor arc directions) and any known seismic wave is predicted to arrive in the same time window and along the same backazimuth (i.e. minor or major great-circle path) (e.g Fig. 4d). Of all identified signals, only 2% match the time and direction predicted for known seismic phases, and thus are discarded.

The wavefield may also be contaminated by foreshocks or aftershocks to the analysed events, thus we exclude from further analysis any scattered signals where any magnitude ≥6 earthquake occurs within two hours of the origin time of the studied earthquake (11% of identified scattered signals). As a further test we remove any scattered signal that could be contaminated by a magnitude ≥5 event but find no systematic difference in the distribution of scattering heterogeneity. Our focus on core wave arrivals with slownesses from 2.1 to 4.4 s/deg helps to exclude contamination from smaller, closer events, which have higher slownesses associated with more horizontal incoming energy (and the discarding of GCP signals further minimizes energy from small local events contributing to data we analyse). Therefore, we are certain that our data selection prevents any contamination of the results by local and regional events. Lithospheric scattering directly beneath the array may redirect high slowness contaminating energy to lower slownesses typical of mantle scattering that we consider here. However, the direct contaminating wave would arrive in the same time window as the lithospheric scattered energy, and would likely be more coherent with an obviously inappropriate slowness. This allows a straightforward identification (and removal) of energy scattered from lithospheric structure.

After contaminated time windows have been removed, scattered signals are identified. We pick time windows containing energy prominently above the background noise level in f-k space and consistent with the directivity criteria for P′•P′ scattering (e.g. Fig. 4b). We identify the slowness and back-azimuth of the scattered signal, and select the time at the middle of the 50 s long window as

scattered travel time; therefore, we only identify one scattered signal per 50 s window. If multiple P′•P′ signals are observed in the same time window we retain the signal with the highest coherence, as this will be the best spatially resolved. Multiple waves arriving at a similar time, either scattered or direct, may interfere causing the apparent arrival direction of energy at the array to be incorrect. The apparent signal would likely appear blurred across directions, thus we only select signals with tightly resolved slowness and back-azimuth (within the capabilities of the array).

The back-azimuth, slowness, and time information for each scattered signal are used to calculate a scattering location in the mantle. The back-azimuth of a signal indicates the horizontal direction along which the wave travelled while the slowness defines a discrete path for a 1D Earth model, and the travel-time relates to the scattering depth (Fig. S1). Thus there is a trade-off between the distance and depth of a scattered path, hence we attempt to fit both slowness and travel-time simultaneously with a grid search. We ray trace backwards from the array along the observed back-azimuth to a range of possible scattering depths and distances, and then ray-trace from these scattering locations to the source. Possible scattering locations are spaced every 0.01° in distance between the minimum and maximum possible path lengths of PKP along the resolved back-azimuth and 50 km in depth from the CMB to the surface. We model the scattering location by minimising the misfit between the calculated slowness and time for each potential scattering location and the observed values. Mapped scattering heterogeneity locations are discarded if traced rays to the solution location do not well fit the observed

316 slowness and time: if the squared slowness misfit (observed minus predicted) plus
317 twice the squared time misfit is greater than 10, i.e. a weighting factor of 2 is used
318 for travel time misfit and therefore we favour fitting scattering locations with small
319 travel-time misfits. The misfit value selected fits signals within the slowness
320 resolution limit of the arrays. Overall, of the original 4319 identified scattered
321 signals, we discard signals contaminated by other events (11% of the original
322 population), other phases (2%), and poorly fit signals (44%), leaving 1876 mapped
323 scattering heterogeneities.

324 Due to the uncertainty in travel-time (from using the middle of the 50 s time
325 window) and the uncertainty in slowness (due to the ability of the arrays to resolve
326 the incoming direction) we determine the dimensions of the region that contains the
327 heterogeneity based on these limitations. We calculate scattering locations for
328 signals arriving at the start and end of the 50s time window, and with slowness
329 variation of ±0.3 s/deg relative to that measured at the array (estimated from the
330 slowness spacing of the grid-search). This defines a region around the best fitting
331 heterogeneity location that is, on average, ±100 km laterally and vertically. For mid-
332 mantle scattering at high slowness values (~1000-1800 km depth), the error
333 regions can occasionally grow to values as large as ±800 km laterally and ±500 km
334 vertically but this larger misfit is only relevant for around 5% of the solution
335 scattering locations, thus the majority of the scattering heterogeneities identified in
336 our dataset are located to within ±100 km vertically and laterally.

337 Sub-surface structure beneath the majority of the arrays used in this study
338 has been demonstrated to have an insignificant effect on the resolved slowness and

339 back-azimuth (Bondar et al., 1999). Nevertheless, removing scattering
340 heterogeneities observed at Chiang Mai array, which is most affected by sub-surface
341 structure, dominantly reduces scattering in the upper 200 km of the mantle and
342 causes no significant change in our conclusions on the relationship with lower
343 mantle structure.

344

345

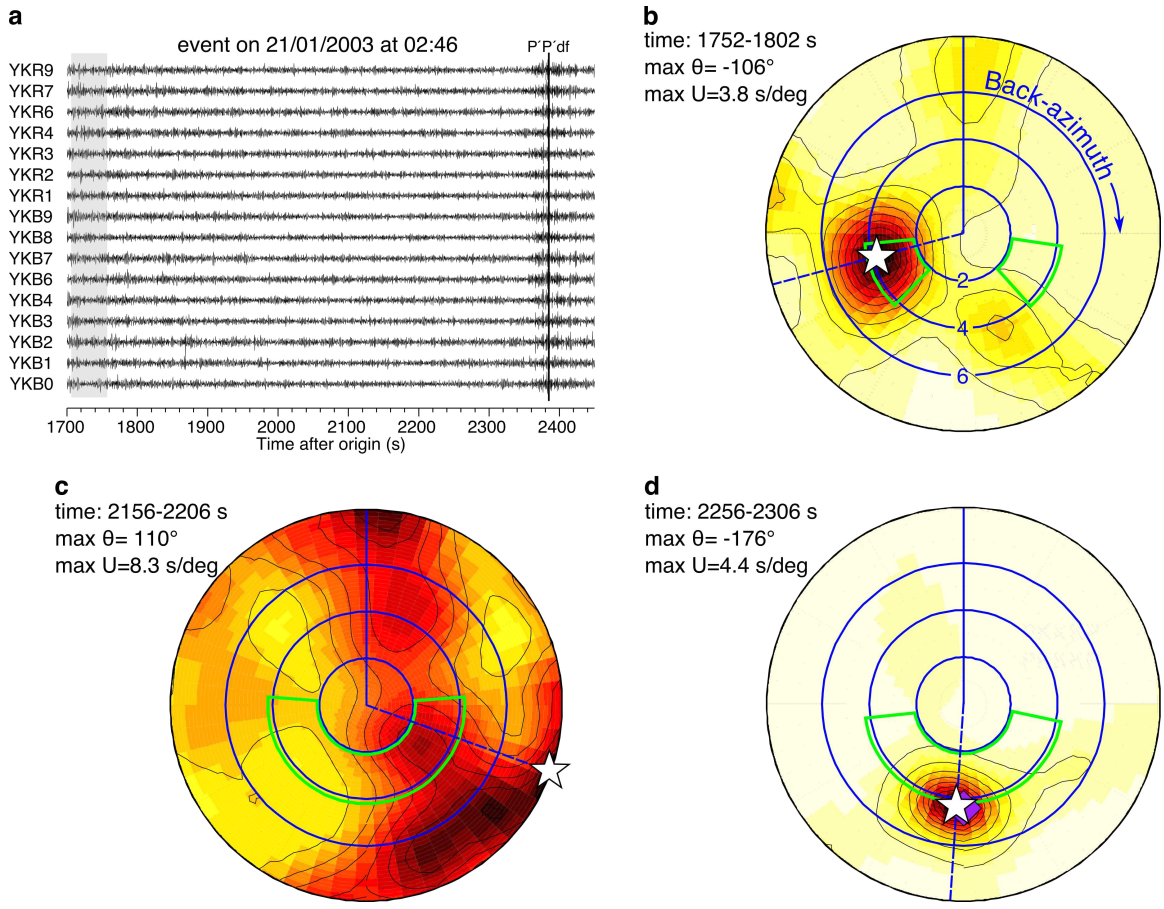

346
347 **Figure 4:** Array data are shown for (**a** and **b**) a magnitude 6.5 event, 24 km depth,
348 52° away from Yellowknife array, and (**c** and **d**) a magnitude 7.8 event, 0 km depth,
349 37° away from Warramunga array. **(a)** The time window for P′•P′ scattering (1700-
350 2450 sec for this event, blue region in Fig. 2). The predicted time of the direct phase,
351 $P'P'_{df}$, is shown by the vertical line, marking the end of the scattering window used
352 here. Data are filtered between 0.5 and 2.0 Hz. The grey shaded time window

corresponds to information shown in **(b)**. **(b)** f-k processing of the 50 sec time window shown grey in **(a)**, displayed in terms of back-azimuth (θ, azimuthal axis) and slowness (u, radial axis outwards from 0 to 8 s/deg with rings marking 2 to 6 s/deg). Back-azimuth is measured relative to the great-circle path (vertical blue line). The white star shows the maximum coherence in the f-k analysis, arriving with relative back azimuth = -106° (blue dashed line). The 90% coherence contour is roughly ±10° wide in back-azimuth and ±0.5 s/deg in slowness around the maximum. The green regions show the range of possible slownesses and back-azimuths for P′•P′ waves scattering at this distance and the median depth of scattering for this time window (from the shape of the potential scattering regions, grey regions in Fig. 3). **(c)** f-k processing of a time window showing no clear P′•P′ waves. (**d**) f-k processing of a time window that is likely contaminated by the direct phase PKKKP (predicted slowness and back-azimuth marked by purple diamond). Time windows (**c**) and (**d**) are not picked for further processing.

[2 COLUMN FIGURE]

4. Results

The mapped locations of scattering heterogeneities are unevenly distributed in the mantle, both laterally and with depth. This is not unexpected given that the potential sampling capacity of our dataset also varies in location and depth (Fig. 3). We divide the number of mapped scatterers by the potential sampling density (Fig. 3) in order to compare relative scattering density for different regions. This normalised scattering population shows that heterogeneities are distributed throughout the mantle, but more abundant scattering heterogeneity is present in the uppermost and lowermost mantle (Fig. 5). The radial scatterer distribution also shows a small increase in scattering heterogeneity between 600 and 900 km depth,

just below the transition zone, and a minimum in the mid-mantle between 1400 to 1800 km depth.

We find that the radial abundance of small-scale scattering heterogeneity matches the RMS amplitude of large-scale tomographic velocities (Fig. 5): scattering is most common and the RMS variation of tomographic velocities is highest in the uppermost and lowermost mantle. This correlation holds roughly for all tomographic models (Fig. S2).

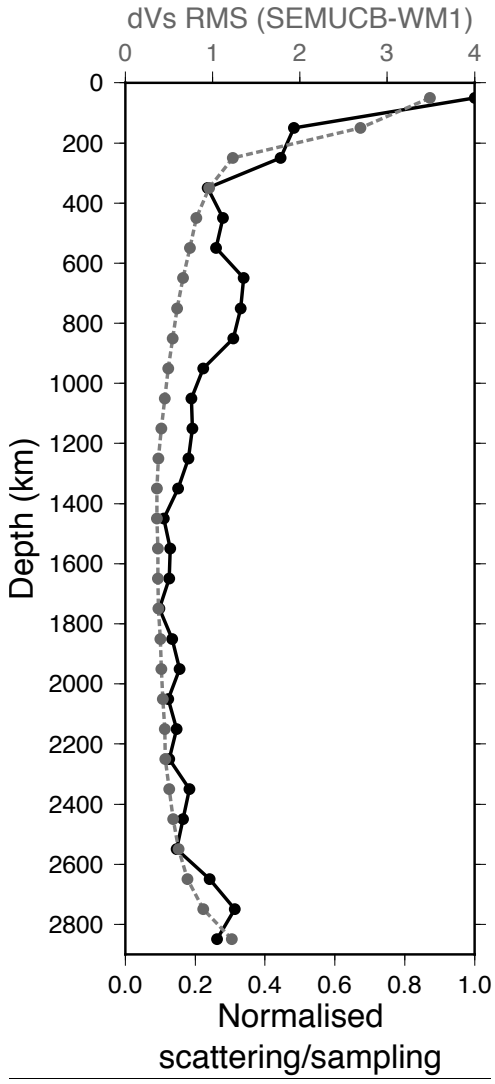

Figure 5: Normalised scattering heterogeneity density with depth (number of scatterers divided by number of samples in each 100 km thick layer) for the complete dataset (black, lower x-axis) and RMS of the shear velocity perturbations from the global tomographic model SEMUCB-WM1 (grey and dashed, upper x-axis) [French and Romanowicz, 2014]. The depth distribution of small-scale scattering heterogeneity roughly correlates with the RMS of long-wavelength dVs perturbations. Both lines are scaled to fit the same axis.
[SINGLE COLUMN FIGURE]

We investigate possible spatial correlation between the resolved scattering heterogeneities and large-scale mantle features, which may be interpreted as proxies for dynamic processes, as in Frost et al., [2017]. We compare the location of scattering heterogeneity to geographical regions beneath hotspots, subducted slabs, regions of high and low tomographic velocities, and regions of high and low lateral tomographic velocity gradients. The high/low velocities and gradients from tomographic models likely relate to the locations of LLSVPs and subducted slabs in the mantle. The spatial locations of scattering heterogeneities are shown, normalised by sampling, in the Supplementary Material, while the absolute latitude, longitude, and depth information for each scattering heterogeneity is shown in Supplementary Table 1

4.1 Relationship between scattering heterogeneities and mantle structure

We compare the distribution of scattering heterogeneity with S-wave tomographic models, both because they are the basis for the definition of the Large

Low Shear Velocity Provinces, and also show consistency between models [Garnero et al., 2016]. We use several tomographic models: GyPSuM [Simmons et al., 2010], SEMUCB-WM1 [French and Romanowicz, 2014], S40RTS [Ritsema et al., 2011], and TX2011 [Grand, 2002]. Additional comparisons with P-wave models are shown in the supplementary material (Figs. S7-9). We calculate lateral velocity gradients from tomographic models, revealing abrupt changes in mantle structure, which thus serve as a proxy for boundaries of the LLSVPs [Thorne et al., 2004, Garnero et al., 2016]. We calculate gradients over a distance of 10° as the resulting gradients well replicate the margins of the LLSVPs found in forward modelling studies [Garnero et al., 2016 and references therein].

We use hotspots from the study of Courtillot et al. [2003]. French and Romanowicz [2015] analysed the tomographic model SEMUCB-WM1 [French and Romanowicz, 2014] and characterised hotspots based on associated tomographic velocity anomalies. We use the 20 hotspots that were labelled as either “primary” or “clear” meaning that the hotspot overlies a column of low velocities from the CMB to 1000 km depth with dVs less than -1.5% or less than -0.5 %, respectively.

We use slab locations from the Regionalized Upper Mantle (RUM) model, which locates slabs at depth using intra-slab seismicity [Gudmundsson and Sambridge, 1998]. When comparing with scattering heterogeneity locations we use slab locations at the surface (zero depth). Slabs move only a small amount laterally as they subduct (≤5° relative to the plate boundary at the surface [Steinberger et al., 2012]), which is unlikely to strongly influence our correlations.

To account for differences in the magnitude, range, and pattern of velocity anomalies and velocity anomaly gradients between tomographic models, and differences in the number of locations in of maps of hotspot and slab locations, we convert maps of tomographic velocities to maps of percentage cumulative area on a sphere sorted by decreasing velocity anomaly (from fast to slow). For example, the 20% area corresponds to the area of the 20% highest tomography velocities of a given depth shell (Fig. 6). We only consider the regions of the tomographic models that match the regions sampled by the P′•P′ dataset at each depth. In this way, the highest and lowest velocities in several tomographic models with inherently differing amplitudes of velocity variation can be directly compared. We establish geographical area percentages associated with the locations of hotspots and subducted slabs by computing the cumulative area surrounding the features within specific distances from them (within the area sampled by the P′•P′ dataset). For example, the first 20% area for slabs corresponds to the region closest to slabs that adds up to 20% of the Earth's surface area; conversely the last 20% area indicates that amount of surface area furthest from slabs.

To estimate correlations between the abundance of small-scale scattering and subducted slabs, hotspots, tomographic velocities and gradients, we compare the location of these features to the distribution of scattering heterogeneity. For each 100 km depth shell, we count scattering heterogeneities in each 20% area division from the feature of interest. To account for the variability in sampling coverage of our dataset (Fig. 3), we count our estimation of potential scatterers (afforded by our event-array distributions) in the same 20% area regions, and

463 calculate the ratio of the number of observed-to-potential heterogeneities. This
464 allows us to construct a map of normalised scattering prevalence, thus effectively
465 removing the bias of our uneven sampling.

466 The first set of comparisons is displayed in Fig. 7 as a cumulative histogram
467 as a function of depth. In the upper 200 km of the mantle, scattering heterogeneities
468 are most common in regions of high velocity (Fig. 7a), which is evident from the
469 horizontal width of the light and dark blue shading being greater than the width of
470 the light and dark red shading over the same depth range. In the lower mantle,
471 especially in the deepest 500 km or so, the opposite is true: scattering
472 heterogeneities are more abundant in low velocity regions (as evident by wider red
473 shading). Regions of the lowermost mantle with high seismic velocities show
474 virtually no correlation with scattering heterogeneities. Scattering is slightly more
475 common in regions of high seismic velocity between 600 and 900 km depth.

476 In the deepest 200 km of the mantle, scattering heterogeneities are more
477 common in regions of high lateral seismic velocity gradients (Fig. 7b: the width of
478 the black and dark blue shading is significantly greater than the light green colors).
479 In the lowest ~1000 km of the mantle, scattering heterogeneities are in greater
480 abundance in the 20% area around hotspots than in any other bin; there is also a
481 slight increase in mapped heterogeneities beneath hotspots in the mid-mantle
482 between 600-900 km depth (see the wide red colors shading, Fig. 7c). Our mapped
483 scattering heterogeneities show little correlation with regions surrounding the
484 surface location of slabs, except in areas furthest from slabs in the 600-900 km
485 depth range (indicated by the wide orange-yellow shading, Fig. 7d). In the upper

200 km of the mantle, scattering strongly correlates with high seismic velocities and proximity to slabs (Figs. 7a and 7d, blue and yellow shading, respectively), which, at these shallow depths is most closely related to the location of continents. While the precise locations of the heterogeneities is different, the heterogeneities resolved with P′•P′ show a very similar distribution in the lowermost 300 km of the mantle to those heterogeneities resolved with PK•KP in an earlier study [Frost et al., 2017].

To test the robustness of these correlations we determine how likely they are to have been produced by chance. We rotate the tomographic models (of velocity and lateral gradient), and hotspot and slab locations by a random angle about a randomly located pole of rotation. We then recompute the correlations between the rotated geographical features and the distribution of the unrotated scattering heterogeneities. The random rotation is repeated 200 times for each tomography model, as well as for the hotspot and slab locations, to calculate the range of possible correlations. The mean and standard deviation of the range of correlations at each depth is computed, assuming Gaussian statistics. We compare this with the original, unrotated data in Fig. 8, and consider any correlation to be statistically significant if the correlation value between scatterers and regions of the unrotated phenomena plots outside one standard deviation from the mean correlation of the rotated phenomena (demonstrating that at least 84% of the random correlations are a lower value). When we do not assume a distribution and instead calculate the proportion of samples above and below one standard deviation of the data, we find very similar patterns of significant observations. Using this metric, we define the following correlations as significant and unlikely the product of chance:

(1) An increased correlation with scatterers in regions of low velocity at depths greater than 1800 km (solid red line in the left panel of Fig. 8a)

(2) An increased abundance of scattering heterogeneities in regions of high velocity gradient in the deepest few hundred km of the mantle, as well as between 1600-2000 km depth (solid red line in the right panel of Fig. 8b).

(3) An increased abundance of heterogeneities close to surface hotspot locations at depths greater than 2100 km depth (solid red line in left panel of Fig. 8c).

(4) A decreased abundance of heterogeneities far from surface hotspot locations at almost all depths greater than 800 km depth (solid red line in right panel of Fig. 8c).

There is no significant correlation seen between scatterer locations and slab locations, except an increase in correlation between heterogeneities and large distances from slabs between 600 and 900 km depth, which matches the depth range of the increased correlation with low velocity gradients (solid red lines in left panel of Fig. 8b and right panel of 8d), and an increased correlation between heterogeneities and large distances from slabs throughout much of the lower mantle (which is what one expects if correlations are strong for low velocities).

4.2 Dependence upon choice of model

When comparing small-scale scattering locations with tomographically derived high or low velocities, the results may depend upon the choice of the tomography model. In our previous analysis, we compared the distribution of scattering heterogeneities to tomography model SEMUCB-WM1 [French and Romanowicz, 2014]. We further explore the relationship between our mapped fine-

scale scattering heterogeneities with large-scale structures in other tomography models: GyPSuM, S40RTS, and TX2011 (Figs. S4-6 and S7-9 for P-wave models). We find small differences in precise depths and magnitudes of correlations with different models, but the correlation between scattering and low velocities at depths below 1600 km, and with high velocities at depths of 200 km and shallower and the robustness of these correlations are consistent between models.

To test the dependence of correlation on the pattern of hotspots, in addition to comparing with rotated hotspot locations, we create a population of randomly located hotspots, equal in number to the primary and clear hotspots from Courtillot et al., [2003] and French and Romanowicz [2015]. We find that a synthetic population generates no preferential spatial correlation with the scattering heterogeneities (Fig. S10). Furthermore, when the population of random hotspot locations is rotated to test the robustness of the correlation, the correlation of the random population very often falls well within the one standard deviation range of the rotated data (Fig. S12). This implies that the observed correlation between hotspot locations and scattering heterogeneities in the lower mantle is caused by the specific distribution of hotspots.

We test the influence of our decision to use only the surface slab locations of the RUM model. We calculate the spatial correlation between scattering heterogeneities and slab locations as described above, but use slab locations at the depth of the heterogeneity. When considering scattering heterogeneities at depths greater than that which the slab is mapped to we use the location of the slab at the last mapped depth and project this position vertically down to the CMB. This

556 method of vertical extrapolation likely still misrepresents the locations of slabs:
557 some amount of lateral movement at greater depths is evident in tomographic and
558 geodynamic models but is typically on the order of a few degrees [e.g. French and
559 Romanowicz, 2014 and Steinberger et al., 2012]. Nonetheless, we find no significant
560 difference in the correlations between using the surface slab location and slab
561 locations with depth (Fig. 7 and Figs. S11 and S12).
562

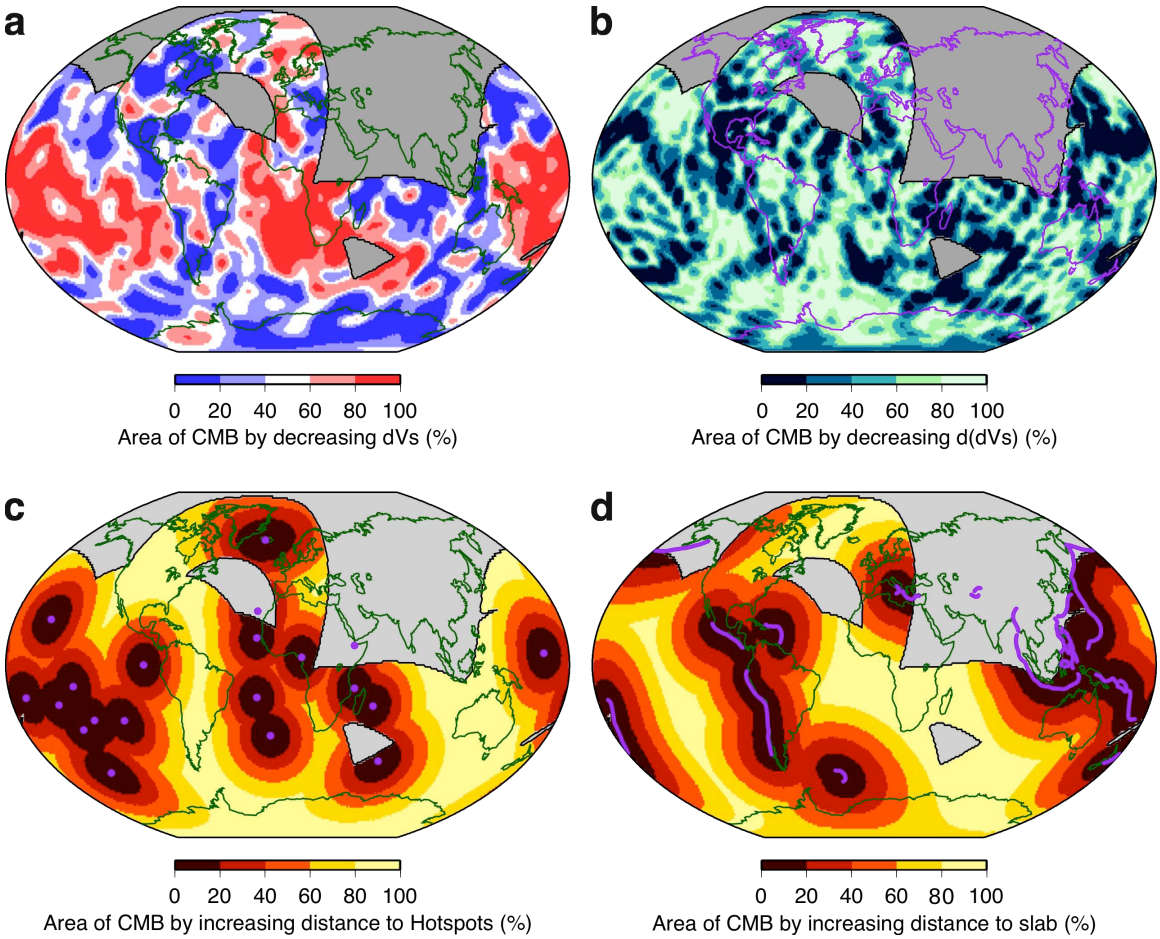

563
564 **Figure 6:** Tomography and distance from subduction zones and hotspots by
565 percentage area calculated for sampling at the CMB. (a) The magnitude of the
566 velocity anomalies in SEMUCB-WM1 [French and Romanowicz, 2014] in the area
567 sampled by our dataset at the CMB displayed by decreasing anomaly (from fast blue

areas to slow red areas) in regions occupying 20% of the area of the CMB. (b) The magnitude of the lateral velocity gradient decreasing from high to low in 20% area regions. (c) Distance from hotspots (connected to plumes identified as either primary or clear in the analysis of French and Romanowicz [2015]). (d) Distance from slabs (at zero depth slice in RUM [Gudmundsson and Sambridge, 1998]. Black line marks the extent of the sampled area (as in Figure 3d).

[2 COLUMN FIGURE]

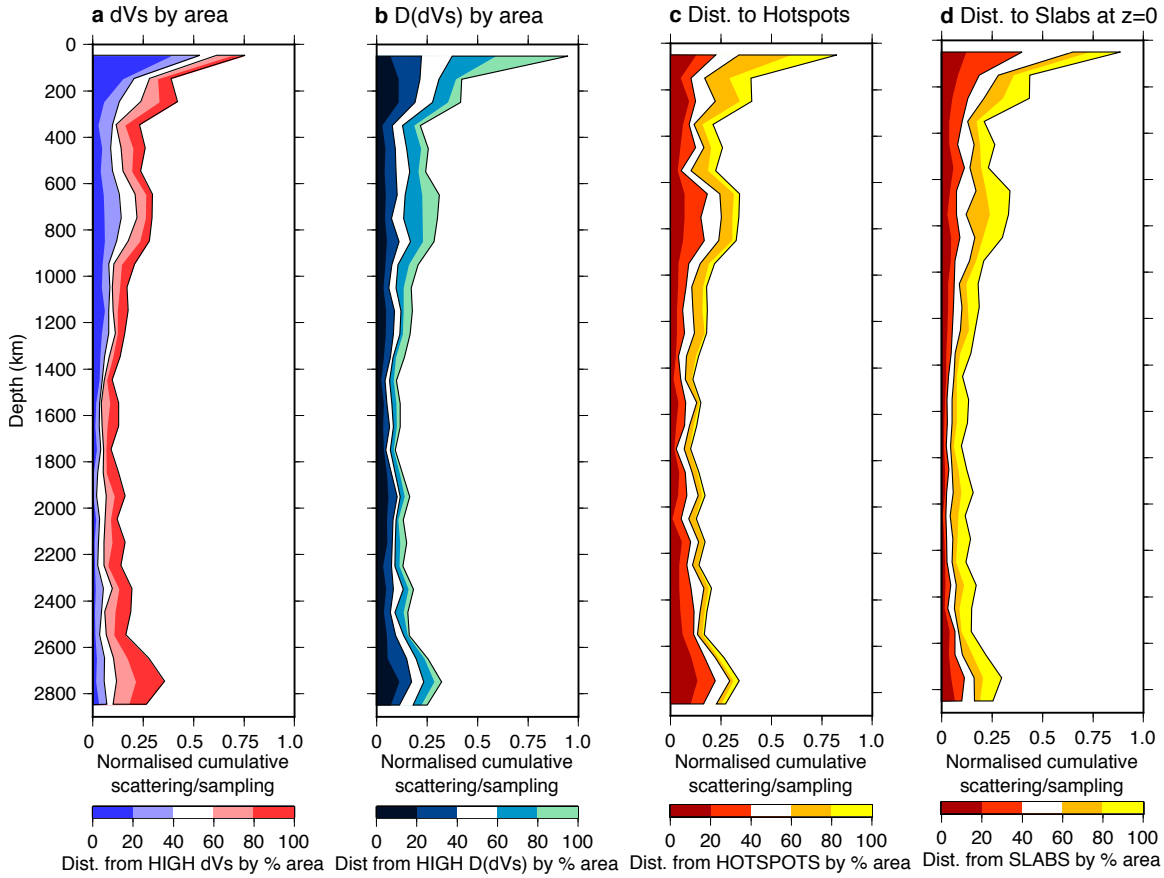

Figure 7: Scattering abundance (bar width) with depth compared with the distribution of large-scale heterogeneity throughout the mantle (colour scale). Scattering abundance is calculated cumulatively across all areas, is divided by

sampling, and is normalised to unity, representing the maximum scattering abundance at any depth. **(a)** Scattering heterogeneity and tomographic velocity anomalies (from SEMUCB-WM1 [French and Romanowicz, 2014]) sorted from highest (blue) to lowest (red) measured as a function of surface area in 20% area bins. **(b)** Scattering heterogeneity and lateral tomographic velocity gradient sorted from highest (dark blue) to lowest (light green). **(c)** Scattering heterogeneity and distance from hotspots from low to high (red and yellow, respectively). **(d)** Scattering heterogeneity and distance from slabs from low to high (red and yellow, respectively). Scattering heterogeneity in the lower mantle shows an affinity for both low seismic velocities and hotspots. Black lines encapsulate the highest and lowest 40% area regions.

[2 COLUMN FIGURE]

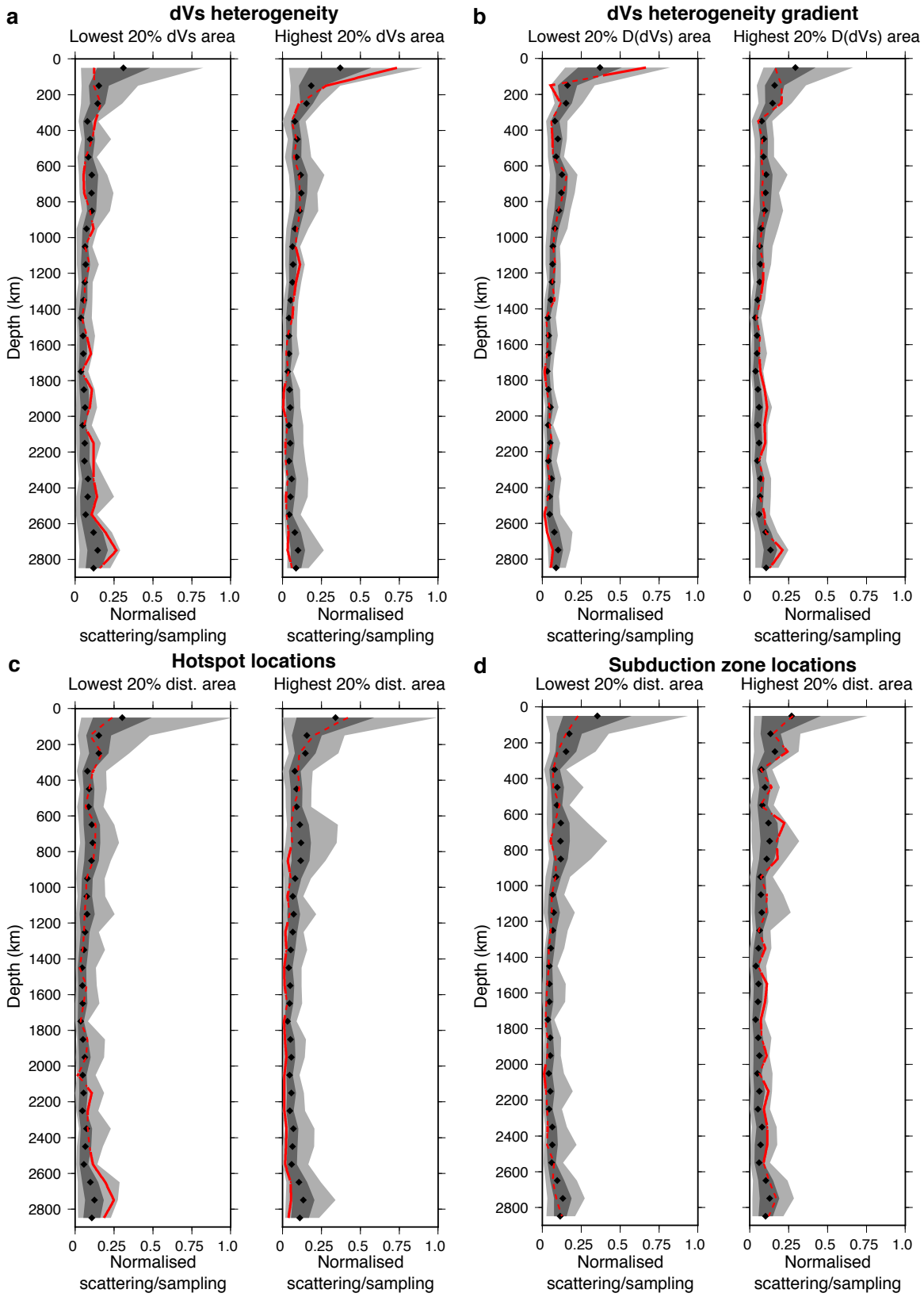

Figure 8: Scattering abundance with depth, divided by sampling, showing the unrotated model (red line) compared with rotated models (grey). The unrotated

model (red line) is dashed when within one standard deviation (dark gray shading) of the mean of the spatial correlations (black diamonds) with the rotated models, and solid when outside this level. The lighter shaded region marks the range of all correlations with the randomly rotated phenomena. Comparisons are shown for: **(a)** tomographically derived velocity heterogeneity from SEMUCB-WM1 for the 20% area corresponding to the lowest (left panel) and highest velocities (right panel). Correlation between increased scattering abundance and low velocities appears robust in the deepest mantle, and correlation to high velocities is robust in the shallowest 200 km of the mantle, as well as around 1200 km depth. **(b)** As in **(a)** except correlations are between observed scattering and rotated shear velocity gradients in model SEMUCB-WM1. Correlations are most significant for the strongest gradients (right panel) at the base of the mantle. **(c)** As in **(a)** except correlations are between scatterers and distance to rotated hotspot regions. Correlations are most significant in the deepest mantle in close proximity to being beneath hotspots (left panel). **(d)** as in **(c)** except correlations are between scatterers and distance to rotated slab regions. Our random rotation test shows no significant correlation between scatterers and proximity to slabs.

[2 COLUMN FIGURE]

5. Discussion

In this study we mapped scattering heterogeneities and explored their geographical relationship to tomographic velocities and gradients, as well as hotspots and slabs. Our results may be interpreted in terms of the distribution of mantle heterogeneity, which we will discuss here.

5.1 Possible origins of scattering heterogeneity in the mantle

We observe scattering from small-scale heterogeneity throughout the mantle, with increased heterogeneity at the top and bottom of the mantle. Seismic waves can be scattered by volumetric heterogeneity with sharp impedance contrasts, when the heterogeneity has a minimum scale length comparable to the wavelength of the incident wave. Our method is not capable of resolving the precise partitioning of the incident wavefield into scattered versus transmitted energy, since we do not have a consistent reference phase to compare to the amplitude of the scattered wave. Thus we are unable to constrain the properties of the heterogeneities (e.g. impedance contrast). Nonetheless, the frequencies of waves that we study (between 0.5 and 2.0 Hz) imply that observed scattering heterogeneities have a minimum scale length of one to tens of km.

A variety of structures could scatter the energy observed in our data. We can use the distribution and sizes of scattering heterogeneities to address the feasibility of possible causes. Material undergoing phase changes such as from bridgmanite to post-perovskite (pPv) in the lower mantle (or the back transformation) [Murakami et al., 2004; Oganov and Ono, 2004], as well as transitions of olivine to wadsleyite to

642 ringwoodite to perovskite through the upper mantle transition zone could provide
643 an impedance contrast with the ambient mantle. The bridgmanite to pPv phase
644 transition is predicted to occur in the deepest few 100 km of the mantle, and only in
645 relatively cold regions of the mantle for a standard pyrolitic composition, thus
646 would not be appropriate to explain scattering at all depths and locations, unless
647 mineralogical alterations are considered [Lay et al. 2006]. The phase transition is
648 controlled by temperature, composition, and pressure. While pressure is assumed
649 hydrostatic, local changes in composition, perhaps by contamination of the mantle
650 by subducted mid-ocean ridge basalt (MORB), may influence the pPv transition
651 [Grocholski et al., 2012], possibly causing the transition to occur locally in the
652 vicinity of the MORB contamination. Metastability of phase transitions due to
653 chemical heterogeneity [Catalli et al., 2009] could allow transformed minerals to
654 persist outside of their expected stability range. High thermal conductivity in the
655 lower mantle [Stackhouse et al., 2015] renders small-scale temperature changes an
656 unlikely cause of spatially limited occurrence of the pPv transition. While many
657 morphologies and scale lengths of pPv regions can be envisioned that could
658 contribute to wave field scattering observed here, the details of such processes are
659 not constrained. However, pPv should not be stable in the upper mantle, and thus
660 cannot explain observed scattering there. Nonetheless, pPv remains a viable
661 contributor to wavefield scattering in the deepest mantle.

662 The subduction process continuously introduces compositional
663 heterogeneity into the mantle. Scattering has previously been mapped in the upper
664 mantle and lower mantle in the proximity of subduction zones [Kaneshima and

665 Helffrich, 1998; Rost and Earle, 2010; Miller and Niu, 2008; Bentham and Rost,
666 2014]. We do not observe a robust preference of scattering heterogeneity in upper
667 mantle regions of subduction over other regions. While we do observe slightly
668 increased scattering in regions associated with subduction at around 600 to 900 km
669 depth (Fig. 7a), this does not appear to be statistically significant (Fig. 8a, right
670 panel). Nonetheless, the increased concentration of scattering heterogeneity
671 between 600 and 900 km depth shows robust spatial correlation with regions away
672 from subduction zones and areas of low amplitude lateral velocity gradient (Figs. 7
673 and 7). In some tomographic models subducting slabs are observed to flatten at a
674 similar depth, between ~800-1200 km depth [e.g. French and Romanowicz, 2015].
675 Oceanic crust may be responsible for scattering throughout the mantle.
676 Subducted oceanic crust may remain unmixed due to slow chemical diffusion rates
677 [Olson et al., 1984] and is only homogenised into the mantle through mechanical
678 stirring. If the observed scattering heterogeneities are oceanic crust then the
679 dispersal of heterogeneities throughout the mantle must be faster than stirring and
680 removal of heterogeneities since scattering heterogeneity is also observed in
681 regions that have not been influenced by subduction for a long time.
682 The iron spin transition affects the velocity and density of iron-bearing
683 mantle materials [Lin et al., 2005]. Recently, this has been observed to occur over a
684 60 GPa pressure range (~600 to 2000 km depth) [Holmstrom and Stixrude, 2015]
685 and thus would likely not generate discrete heterogeneities capable of causing
686 scattering.

687 Products of chemical reactions between core and mantle materials are
688 predicted to have physical properties in contrast with the ambient mantle [Knittle
689 and Jeanloz, 1989] thus may be capable of causing seismic scattering. Experiments
690 demonstrate that such mantle material enriched in iron would likely be denser than
691 the ambient mantle [Wicks et al., 2010]. An interesting possibility is the
692 development of a reaction product layer that would inhibit further interaction with
693 the core; for this case, products are likely to be constrained to a very limited
694 thickness close to the CMB, on the order of a few meters to kilometers [Kanda and
695 Stevenson, 2006]. However, flow in the deep mantle could generate thicker
696 accumulations of reaction products [Mao et al., 2006], which could scatter waves. In
697 addition, ULVZs are commonly imaged to have vastly reduced seismic velocities of
698 up to -10% dVp and -30% dVs, and increased density of +10-20% relative to the
699 surrounding mantle [e.g., McNamara et al., 2010]. Partial melt of mantle material has
700 been proposed as an explanation of ULVZs [Williams and Garnero, 1996]. Partial
701 melt may be denser than the solid state [Ohtani and Maeda, 2001] as well as having
702 strongly reduced seismic velocities. While ULVZs and CMB reaction products could
703 explain deeper scattering heterogeneities, simulations have suggested that dense
704 material may also be entrained up to 200 km above the CMB, dependent on density,
705 viscosity, and vigor of mantle flow [Bower et al., 2011]. CMB topography or
706 roughness might cause scattering [Chang and Cleary, 1981; Mancinelli et al., 2016],
707 but this could not explain heterogeneities we map up off of the CMB throughout the
708 mantle. LLSVPs may be compositionally distinct from the surrounding mantle [e.g.
709 Garnero et al., 2016], and dynamical flow models predict that the LLSVP material

710 will be gradually entrained into mantle flow on small length scales [Li et al., 2014;
711 Williams et al., 2015; Mulyukova et al., 2015]. Thus, depending on the LLSVP
712 properties and entrained heterogeneity scale, this process might give rise to
713 scattering. Geodynamic models also predict that surrounding ambient mantle
714 material can be downward entrained into the LLSVPs, thus offering an origin of
715 scattering within LLSVP regions.

716
717 *5.2 Distribution of scattering heterogeneity*
718
719 The distribution of small-scale volumetric heterogeneities is likely strongly
720 dependent on the dynamic properties and processes within the Earth. In numerical
721 simulations of mantle dynamics small-scale heterogeneity, particularly that derived
722 from subducted oceanic crust, tends to be concentrated in regions of upwelling from
723 the lower mantle around plumes and downwelling from the surface around
724 subduction zones (Fig. 1 of Li et al., [2014]). The same focusing beneath upwellings
725 is expected for basal heterogeneities [McNamara et al., 2010] (e.g., compositionally
726 distinct ULVZ material, CMB reaction products, and entrained LLSVP material).
727 Furthermore, large-scale mantle heterogeneity may influence radial small-scale
728 heterogeneity distribution by modifying the convective flows in which the
729 heterogeneities could be entrained [Li et al., 2014].

730 As wavelength at some fixed frequency is a function of the local velocity,
731 which changes with depth, and the wavelength of scattering structure that can be
732 resolved is dependent on the incident frequency, it follows that in band limited data,
733 the resolvable scattering wavelength changes with depth. We filter all data between
734 0.5 and 2.0 Hz, therefore, we resolve scattering heterogeneity with wavelengths

735 between about 7-28 km at the CMB, decreasing to about 3-12 km at the surface.
736 Stirring of initially larger-scale heterogeneity is suggested to lead to a cascade of
737 heterogeneity sizes, increasing in abundance with decreasing scale [Olson et al.,
738 1984]. A previous study of the scale of scattering heterogeneities in the lowermost
739 mantle found the most common scale-length to be 4-7 km, but other scales were
740 also present [Frost et al., 2017]. Despite the limited frequency range used in this
741 study, we are likely imaging heterogeneity of a similar size (around 7 km)
742 throughout the mantle.

743 The similarity between scattering heterogeneity abundance and tomographic
744 amplitude (Fig. 5) may arise from processes relating to convection and chemical
745 differentiation that likely generate strong lateral velocity variations on continental
746 scales and smaller through stirring and diffusion. Lower mantle anomalies manifest
747 at a range of spatial scales (LLSVPs, ULVZs, D′′, CMB reaction products), and stirring
748 and entrainment may further decrease their size [Olson et al., 1984, Li et al., 2014],
749 leading both to high-amplitude large-scale velocity anomalies and abundant small-
750 scale scattering. Upper mantle heterogeneity related to subduction, magmatism, and
751 convective processes are also likely to occur across scales. In addition to increased
752 scattering at the top and bottom of the mantle, we also observe a slight but marked
753 increase in scattering abundance from 600-900 km depth, independent of the
754 tomographic velocity structure, which may relate to slab subduction processes or
755 large-scale vertical viscosity changes [Rudolph et al., 2015].

756
757 **6. Conclusion**
758

759 Through analysis of the high-frequency seismic wavefield we map the
760 distribution of small-scale seismic heterogeneity, on the order of ~1-10 km in size,
761 throughout Earth's mantle. We deterministically locate vastly more scattering
762 heterogeneities than has been done previously, significantly improving our
763 understanding of small-scale mantle structure. The spatial distribution and scale-
764 length of this scattering heterogeneity suggests it may be the product of several on-
765 going processes in the mantle. These include oceanic crust disseminated throughout
766 the mantle, entrainment of basal heterogeneities such as ULVZ material or core-
767 mantle reaction product, and compositionally distinct LLSVP material swept into
768 mantle flow. Subducted MORB may suitably explain all scattering observations
769 without scattering contributions from other sources. However, we cannot rule out
770 that scattering is caused by a mixture of heterogeneities with different origins in
771 different regions and depths. While small-scale heterogeneity appears present in
772 much of the mantle, we find increased scattering heterogeneity within the
773 uppermost 200 km of the mantle and the lowermost 300 km of the mantle, similar
774 to heterogeneity amplitudes seen in tomography models. We find no statistically
775 significant correlation between scattering and subducting slabs in the upper 1000
776 km of the mantle. In the lower mantle (from around 1500 km depth down to the
777 CMB), scattering is most common in regions related to the LLSVPs and close to
778 deeply sourced mantle hotspots. Meanwhile, scattering is rare in regions far from
779 deeply sourced mantle hotspots. This suggests that large-scale convective lower
780 mantle structures may entrain and concentrate small-scale heterogeneity in regions
781 of upwelling, downwelling, and stagnant flow.

Acknowledgements: This work was supported NSF grant EAR1401270 and NERC grants NE/K006290/1 and NE/H022473/1. CTBT International Monitoring System data used here were acquired while the author was undertaking a studentship sponsored by the UK National Data Centre at AWE Blacknest. The paper benefited from discussions with Barbara Romanowicz, and improved from helpful comments of two reviewers.

References:

Bentham, H. L. M. & Rost, S. Scattering beneath Western Pacific subduction zones: evidence for oceanic crust in the midmantle. Geophysical Journal International 197, 1627–1641 (2014).

Blandford, R. R. An automatic event detector at the Tonto Forest seismic observatory. Geophysics 39, 633–643 (1974).

Bower, D. J.,Wicks,J.K.,Gurnis,M. & Jackson, J. M.A geodynamic and mineral physics model of a solid-state ultralow-velocity zone.Earth Planet. Sci. Lett. 303,193–202 (2011).

Bondar, I., North, R.G., Beall, G., 1999. Teleseismic slowness-azimuth station corrections for the International Monitoring System seismic network. Bull. Seism. Soc. Am.89, 989–1003.

Brandenburg, J. P. & van Keken, P. E. Deep storage of oceanic crust in a vigorously convecting mantle. Journal of Geophysical Research 112, 1–15 (2007).

Capon, J., Greenfield, R. & Kolker, R. Multidimensional maximum-likelihood processing of a large aperture seismic array. Proc. IEEE 55, 192–211 (1967).

Catalli, K., Shim, S.-H. & Prakapenka, V. Thickness and Clapeyron slope of the post-perovskite boundary. Nature 462, 782–5 (2009).

Chang, A. C. & Cleary, J. R. Scattered PKKP: Futher evidence for scattering at a rough core-mantle boundary. Phys. Earth planet. Int. 24, 15–29 (1981).

819
820 Cleary, J. & Haddon, R. A. W. Seismic wave scattering near the core-mantle
821 boundary: a new interpretation of precursors to PKP. Nature 240, 549–551 (1972).
822
823 Courtillot, V., Davaille, A., Besse, J. & Stock, J. Three distinct types of hotspots in the
824 Earth's mantle. Earth Planet. Sci. Lett. 205, 295–308 (2003).
825
826 Domeier, M., Doubrovine, P. V., Torsvik, T. H., Spakman, W. & Bull, A. L. Global
827 correlation of lower mantle structure and past subduction. Geophys. Res. Lett.
828 4945–4953 (2016).
829
830 Doubrovine, P. V., Steinberger, B. & Torsvik, T. H. A failure to reject: Testing the
831 correlation between large igenous provinces and deep mantle structures with EDF
832 statistics. Geochem. Geophys. Geosyst. 1130–1163 (2016).
833
834 French, S. W. & Romanowicz, B. A. Whole-mantle radially anisotropic shear-
835 velocity structure from spectral-element wave form tomography. Geophys. J. Int.199,
836 1303–1327 (2014).
837
838 French, S. W. & Romanowicz, B. A. Broad plumes rooted at the base of the Earth's
839 mantle beneath major hotspots. Nature 525, 95–99 (2015).
840
841 Frost, D. A., Rost, S., Selby, N. D. & Stuart, G. W. Detection of a tall ridge at the core-
842 mantle boundary from scattered PKP energy. Geophys. J. Int. 195, 558–574 (2013).
843
844 Frost, D. A., Rost, S., Garnero, E. J. & Li, M. Seismic evidence for Earth's crusty deep
845 mantle. Earth and Planetary Science Letters 470, 54–63 (2017).
846
847 Garnero, E. J., McNamara, A. K. & Shim, S.-h. Continent-sized anomalous zones with
848 low seismic velocity at the base of Earth's mantle. Nature Geosci. 1–9 (2016).
849
850 Grand, S. P. Mantle shear-wave tomography and the fate of subducted slabs. Phil.
851 Trans. R. Soc. Lond A 360, 2475–2491 (2002).
852
853 Grocholski, B., Catalli, K., Shim, S.-H. & Prakapenka, V. Mineralogical effects on the
854 detectability of the postperovskite boundary. Proceedings of the National Academy
855 of Sciences 109, 2275–2279 (2012).
856
857 Gudmundsson, O. & Sambridge, M. A regionalized upper mantle (RUM) seismic
858 model. J. Geophys. Res. 103, 7121–7136 (1998).
859
860 Hedlin, M. A. H., Shearer, P. M. & Earle, P. S. Seismic evidence for small-scale
861 heterogeneity throughout the Earth's mantle. Nature 387, 145–150 (1997).
862
863 Holmström, E. & Stixrude, L. Spin Crossover in Ferropericlase from First-Principles
864 Molecular Dynamics. Phys. Rev. Lett. 117202, 1–5 (2015).

Kanda, R. V. S. & Stevenson, D. J. Suction mechanism for iron entrainment into the lower mantle. Geophys. Res. Lett. 33, 4–7 (2006).

Kaneshima, S. & Helffrich, G. Detection of lower mantle scatterers northeast of the Marianna subduction zone using short-period array data. J. Geophys. Res. 103, 4825–4838 (1998).

Knittle, E. & Jeanloz, R. Simulating the core-mantle boundary: An experimental study of high pressure reactions between silicates and liquid iron. Geophys. Res. Lett. 16, 609–612 (1989).

Lay, T., Hernlund, J., Garnero, E. J. & Thorne, M. S. A post-perovskite lens and D" heat flux beneath the central Pacific. Science 314, 1272–6 (2006).

Li, M., McNamara, A. K. & Garnero, E. J. Chemical complexity of hotspots caused by cycling oceanic crust through mantle reservoirs. Nature Geosci. 7, 366–370 (2014).

Lin, J-f., Struzhkin, V. V., Jacobsen, S. D., Hu, M. Y., Chow, P., Kung, J., Liu, H., Mao, H-k. & Hemley, R. J.. Spin transition of iron in magnesiowustite in the Earth's lower mantle. Nature 436, 377–380 (2005).

Mancinelli, N. J. & Shearer, P. M. Reconciling discrepancies among estimates of small-scale mantle heterogeneity from PKP precursors. Geophys. J. Int. 195, 1721–1729 (2013).

Mancinelli, N., Shearer, P. & Thomas, C. On the frequency dependence and spatial coherence of PKP precursor amplitudes. J. Geophys. Res. 121, 1873–1889 (2016).

Mao, W. L. et al. Iron-rich post-perovskite and the origin of ultralow-velocity zones. Science 312, 564–5 (2006).

McNamara, A. K. & Zhong, S. Thermochemical structures beneath Africa and the Pacific Ocean. Nature 437, 1136–9 (2005).

McNamara, A. K., Garnero, E. J. & Rost, S. Tracking deep mantle reservoirs with ultra-low velocity zones. Earth Planet. Sci. Lett. 299, 1–9 (2010).

Miller, M. & Niu, F. Bulldozing the core mantle boundary: Localized seismic scatterers beneath the Caribbean Sea. Phys. Earth planet. Int. 170, 89–94 (2008).

Mulyukova, E., Steinberger, B., Dabrowski, M. & Sobolev, S. V. Survival of LLSVPs for Billions of Years in a Vigorously Convecting Mantle: Replenishment and Destruction of Chemical Anomaly. J. Geophys. 3824–3847 (2015).

910 Murakami, M., Hirose, K., Kawamura, K., Sata, N. & Ohishi, Y. Post-perovskite phase
911 transition in MgSiO3. Science 304, 855–858 (2004).
912
913 Oganov, A. R. & Ono, S. Theoretical and experimental evidence for a post-perovskite
914 phase of MgSiO3 in Earth's D" layer. Nature 430, 445–448 (2004).
915
916 Ohtani, E. & Maeda, M. Density of basaltic melt at high pressure and stability of the
917 melt at the base of the lower mantle. Earth Planet. Sci. Lett. 193, 69–75 (2001).
918
919 Olson, P., Yuen, D. A. & Balsiger, D. Mixing of passive heterogeneities by mantle
920 convection. J. geophys. Res. 89, 425–436 (1984).
921
922 Ritsema, J., Deuss, A. F., van Heijst, H. J. & Woodhouse, J. H. S40RTS: a degree-40
923 shear-velocity model for the mantle from new Rayleigh wave dispersion, teleseismic
924 traveltime and normal-mode splitting function measurements. Geophys. J. Int. 184,
925 1223–1236 (2011).
926
927 Rost, S. & Earle, P. S. Identifying regions of strong scattering at the coremantle
928 boundary from analysis of PKKP precursor energy. Earth Planet. Sci. Lett. 297, 616–
929 626 (2010).
930
931 Rost, S., Earle, P. S., Shearer, P. M., Frost, D. A. & Selby, N. D. Seismic detections of
932 small-scale heterogeneities in the deep Earth. In Khan, A. & Deschamps, F. (eds.) The
933 Earth's Heterogeneous Mantle, chap. 12, 367–390 (Springer International
934 Publishing, 2015).
935
936 Rudolph, M. L., Lekic, V. & Lithgow-Bertelloni, C. Viscosity jump in Earth's mid-
937 mantle. Science 350, 1349–1352 (2015).
938
939 Selby, N. D. Improved Teleseismic Signal Detection at Small-Aperture Arrays. Bull.
940 seism. Soc. Am. 101, 1563–1575 (2011).
941
942 Simmons, N. A., Forte, A. M. & Grand, S. P. Joint seismic, geodynamic and mineral
943 physical constraints on three-dimensional mantle heterogeneity: Implications for
944 the relative importance of thermal versus compositional heterogeneity. Geophysical
945 Journal International 177, 1284–1304 (2009).
946
947 Stackhouse, S., Stixrude, L. & Karki, B. B. First-principles calculations of the lattice
948 thermal conductivity of the lower mantle. Earth Planet. Sci. Lett., 427, 11-17 (2015).
949
950 Steinberger, B., Torsvik, T. H. & Becker, T. W. Subduction to the lower mantle a
951 comparison between geodynamic and tomographic models. Solid Earth 3, 415-432
952 (2012).
953
954 Tackley, P. J. Mantle Geochemical Geodynamics. In Treatise on Geophysics, chap.
955 7.12, 521–585 (Elsevier B.V., 2015), 2nd edn. edn.

Thomas, C., Weber, M., Wicks, C. W. & Scherbaum, F. Small scatterers in the lower mantle observed at German broadband arrays. J. Geophys. Res. 104, 15073–15088 (1999).

Thorne, M., Garnero, E. J. & Grand, S. P. Geographic correlation between hot spots and deep mantle lateral shear-wave velocity gradients. Phys. Earth Planet. Int. 146, 47–63 (2004).

Waszek, L., Thomas, C. & Deuss, A. PKP precursors : Implications for global scatterers. Geophys. Res. Lett. (2015).

Wen, L. Intense seismic scattering near the Earth's core-mantle boundary beneath the Comoros hotspot. Geophys. Res. Lett. 27, 3627–3630 (2000).

Wicks, J. K.,Jackson,J.M. & Sturhahn, W. Very low sound velocities in iron-rich (Mg,Fe)O: Implications for the core-mantle boundary region. Geophys. Res. Lett. 37, 1–5 (2010).

Williams, C. D., Li, M., Mcnamara, A. K., Garnero, E. J. & Soest, M. C. V. Episodic entrainment of deep primordial mantle material into ocean island basalts. Nat. Commun. 6, 1–7 (2015).

Williams, Q. & Garnero, E. J. Seismic Evidence for Partial Melt at the Base of Earth's Mantle. Science 273, 1528–1530 (1996).

Yao, J. & Wen, L. Seismic structure and ultra-low velocity zones at the base of the Earth's mantle beneath Southeast Asia. Physics of the Earth and Planetary Interiors 233, 103–111 (2014).